Mixing at Cross Junctions in Water Distribution Systems. I: Numerical Study

P. Romero-Gomez[1]; C. K. Ho[2]; and C. Y. Choi[3]

Abstract: The present study investigates solute mixing phenomena at various flow rates within a cross junction, which is commonly found in municipal drinking water distribution systems. Simulations using computational fluid dynamics are employed to model the solute concentrations leaving the junction when one inlet is comprised of clean water while the other inlet carries a solute at $R > 10{,}000$. For a few exemplary cases, the resulting velocity vectors and contours of dimensionless concentration are presented to explain the detailed mixing mechanisms at the impinging interface. The turbulent Schmidt number (Sc_t), an important scaling parameter, is also evaluated. Experimental results were used to assess values of Sc_t for various flow conditions that accurately captured the detailed mixing processes within the junction. The present study clearly indicates that mixing at pipe cross junctions is far from "perfect." Incomplete mixing results from bifurcating inlet flows that reflect off one another with minimal contact time. Improving the existing water quality model based on accurate mixing data and simulations is important not only to predict concentrations of chemical species such as chlorine in water distribution systems, but also to prepare for potential intentional and accidental contamination events.

DOI: 10.1061/(ASCE)0733-9496(2008)134:3(285)

CE Database subject headings: Computational fluid dynamics technique; Mixing; Water distribution systems; Numerical models; Potable water.

Introduction

As water utilities evolve from having the single mission of supplying high quality water to consumers to also ensuring water security, the computer modeling tools used for network analysis will also need to evolve to better simulate transport of chemicals and biological agents. Solute mixing behavior at nodes in modeling tools will impact a wide variety of network analyses, including prediction of disinfectant residuals, optimal locations for water quality sensors, prediction models for early warning systems, numerical schemes for inverse source identification, and quantitative risk assessment. Therefore, accurate modeling of water quality has become an increasingly significant issue in managing water distribution systems.

Due to the complexity of municipal water networks, new computer modeling packages have been developed to simulate the potential hydraulic scenarios in a drinking water system. These packages are capable of performing both steady and extended-period (time-varying) simulations of pressurized pipe network systems. They are composed of two model engines: the hydraulic and the water quality models. Hydraulic models generally meet the needs for water network design through years of development, application, and validation, whereas water quality models have yet to prove their performance, especially in highly interconnected networks. Water quality analysis is always coupled with the outcomes from hydraulic simulations because all chemical or biological species are transported throughout the network by advection and diffusion processes. This conceptual approach is widely used for developing most software tools aimed at modeling and managing drinking water systems. Among the many assumptions made regarding water quality engine codes, Mays (2004) stated that perfect and instantaneous mixing of incoming water occurs at all intersections, such as cross and tee junctions.

Fowler and Jones (1991) first questioned the assumption that "perfect" mixing occurs at various intersections in water distribution systems. Among several other concerns about water quality modeling, the assumption of perfect mixing was regarded as a potentially significant cause of discrepancies between model predictions and actual measurements. Even though no quantification of inaccuracies or corrections were performed, they addressed the need for further studies on this assumption and its role in overall water quality in water networks.

Van Bloemen Waanders et al. (2005) examined chemical transport in network models for pressurized flows at a cross junction. In this study, two adjacent incoming flows with the same Reynolds numbers ($R = 44{,}000$) were mixed at a cross junction and discharged at the same Reynolds numbers. Sodium chloride was introduced as a tracer in one of the inlets whereas tap water entered the other inlet. Further, computational fluid dynamics (CFD) simulations were conducted for this flow configuration. If complete mixing were to occur, each outlet would carry 50% of the incoming NaCl mass rate. However, both experimental and numerical tools showed that complete mixing did not occur; instead,

[1]Graduate Research Assistant, Dept. of Agricultural and Biosystems Engineering, The Univ. of Arizona, Tucson, AZ, 85721. E-mail: pedromer@email.arizona.edu

[2]Research Scientist, Sandia National Laboratories, P.O. Box 5800, MS-0735, Albuquerque, NM, 87185-0735. E-mail: ckho@sandia.gov

[3]Professor, Agricultural and Biosystems Engineering, The Univ. of Arizona, Tucson, AZ, 85721. E-mail: cchoi@arizona.edu

Note. Discussion open until October 1, 2008. Separate discussions must be submitted for individual papers. To extend the closing date by one month, a written request must be filed with the ASCE Managing Editor. The manuscript for this paper was submitted for review and possible publication on January 31, 2007; approved on June 15, 2007. This paper is part of the ***Journal of Water Resources Planning and Management***, Vol. 134, No. 3, May 1, 2008. ©ASCE, ISSN 0733-9496/2008/3-285–294/$25.00.

85 and 15% of the total incoming NaCl mass rate was discharged to the outlets adjacent and opposite to the inlet with the tracer, respectively. Thus, the conclusions drawn from their findings suggested that the simplified assumption of perfect and instantaneous mixing at cross interactions may lead to significant inaccuracies.

Ho et al. (2006) investigated various junction geometries (e.g., cross and double-tee junctions) as well as a 3×3 node network with two sources of water with different NaCl concentrations. Three-dimensional CFD simulations based on the finite-element method were carried out. Reynolds (R) numbers ranging from 5,000 to 80,000 were simulated and validated experimentally. The R numbers for all incoming and outgoing flows were the same at all pipe legs in the single-junction studies, but the R numbers were variable in the network studies. In the CFD simulations, the turbulent Schmidt number (Sc_t) was modified to determine if the resulting turbulent eddy diffusivity could be used to adequately represent mixing at the cross junction. The turbulent Sc_t was adjusted to values in the range of $10^{-3}<Sc_t<10^{-1}$ in order to account for enhanced mixing caused by instabilities and vortical structures along the interface of impinging flows. Reynolds-averaged Navier-Stokes (RANS) results were also compared with those based on large eddy Simulations (LES) (Webb and van Bloemen Waanders 2006). Results from high-fidelity LES models revealed the highly transient nature of the mixing behavior at the intersections, unlike the steady interface simulated with RANS models.

Romero-Gomez et al. (2006) studied a wide range of Reynolds numbers to further generalize these earlier findings. The Reynolds number ratios were defined as the significant dimensionless parameters to determine the mixing ratio at a cross junction under turbulent flow conditions ($R>10^4$). They further integrated CFD results into the EPANET water quality model as an exemplary case. EPANET is a freeware program developed by the Water Supply and Water Resources Division of the USEPA's National Risk Management Research Laboratory (Rossman 2000) which is widely used for research on, and management of, drinking water systems. A 5×4 node water network with three demand points was simulated under steady-state conditions with both the original and corrected EPANET water quality model. Contour plots of NaCl concentration throughout the network showed that spatial concentration patterns were greatly changed upon the implementation of mixing ratios at each junction based on CFD results.

The present work extends the aforementioned study by Romero-Gomez et al. (2006) and investigates the solute mixing phenomena at a cross junction at various flow rate combinations. The primary emphasis here is on the underlying physical principles that govern the transport phenomena of the mixing mechanisms as well as their mathematical modeling and computational simulations. Because the water quality model runs on solutions for the velocity field at the cross junction, the generalization of an important scaling parameter, the (Sc_t), is also investigated. It should be noted that Austin et al. (2007) further focus on the experimental verification of the present study.

Formulation

Dimensionless Parameters and Scenarios

As shown in Fig. 1(a), cross junctions [Fig. 1(b)] are common in modern water distribution network grids. The cross junctions can be simplified to two- and three-dimensional shapes as illustrated in Figs. 1(c and d). In all the cases analyzed in this study, the flow

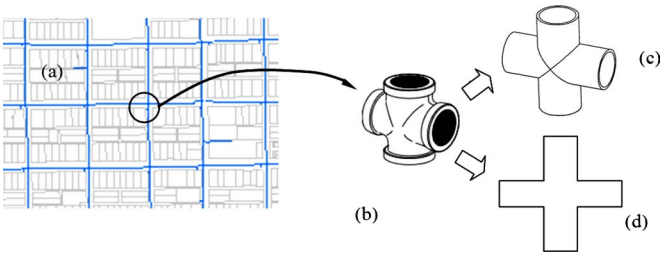

Fig. 1. (a) A water distribution system featuring a cross junction in a midtown neighborhood (Tucson, Ariz.; courtesy of Tucson Water); (b) a typical cross-junction connector; (c) an idealized three-dimensional shape; and (d) a two-dimensional simplification

configuration consisted of two adjacent inlets and two outlets, as depicted in Fig. 2. The pipes were labeled as *W*(west inlet, low concentration water), *S* (south inlet, high concentration inlet), *E* (east outlet), and *N* (north outlet). Sodium chloride (NaCl) was used as a tracer for examining solute mixing. CFD simulations provided highly detailed information of NaCl concentrations throughout the analyzed computational domain. Thus, a weighted-average concentration at the outlets was calculated for each CFD simulation performed. Because varying background tracer concentration can be expected, NaCl concentration was expressed in terms of its dimensionless concentration,

$$C^* = \frac{C_C_W}{C_S - C_W} \tag{1a}$$

It should be noted that C_W corresponds to the background concentration. Eq. (1*a*) was further defined for the north and east outlets.

$$C_N^* = \frac{C_N - C_W}{C_S - C_W}, \quad C_E^* = \frac{C_E - C_W}{C_S - C_W} \tag{1b}$$

It was noted that if "perfect" mixing occurred with equal flows in the four pipe legs, C^* at either outlet automatically would equal 0.5. However, the premise of this research is that dimensionless concentrations can range from 0 to 1 due to the "incomplete" or "split" mixing. It is hypothesized that Reynolds numbers (R)=primary dimensionless parameters driving the mixing at junctions for the given geometry. This suggests that there are an infinite number of combinations of R_S, R_W, R_N, and R_E to describe flow configurations at cross junctions. Therefore, the R

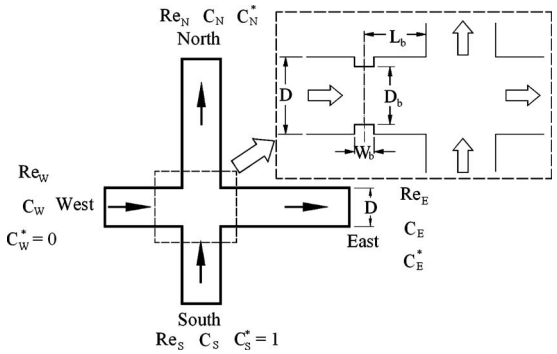

Fig. 2. Hydraulic and water quality configurations of the flow at a cross junction, with detailed geometry of a generic fitting at one of the outlets

ratio of inlet flows ($R_{S/W}$) and the R ratio of outlet flows ($R_{E/N}$) were introduced and used in this work. These provided a generalized application of our findings

$$R_{S/W} = \frac{R_S}{R_W}, \quad R_{E/N} = \frac{R_E}{R_N} \tag{2}$$

Three simplified scenarios were first introduced and the generalized case follows:

- Scenario 1: Equal inflows and outflows ($R_S = R_W = R_N = R_E$).
- Scenario 2: Equal outflows, varying inflows ($R_S \neq R_W$, $R_N = R_E$).
- Scenario 3: Equal inflows, varying outflows ($R_S = R_W$, $R_N \neq R_E$).
- Generalized case: Varying inflows and varying outflows ($R_S \neq R_W \neq R_N \neq R_E$).

There are several reasons to define and investigate both the three proposed scenarios and the generalized case. Scenario I with the same Reynolds numbers at all pipes provides a clear and simplified view of the mixing process at the interface between the two incoming sources of water. Scenarios 2 and 3 were formulated in order to examine broader generalizations of the dimensionless parameters involved in the mixing process. The three scenarios are expected to provide foundations for understanding the generalized case, which defines any real-world flow combinations at cross junctions.

Mathematical Formulation

The steady-state continuity and momentum equations were used to calculate the flow field. The conservation equations are shown in Eqs. (3) and (4), in which $\bar{\bar{\tau}}$=stress tensor that accounts for the effects of viscosity and volume dilation. No mass or momentum sources were considered and gravity effects were neglected

$$\nabla \cdot \bar{u} = 0 \tag{3}$$

$$(\nabla \cdot \bar{u}\bar{u}) = \frac{1}{\rho}[-\nabla P + \nabla \cdot (\bar{\bar{\tau}})] \tag{4}$$

The nature of water flow throughout the network is a function of space and time, it is therefore complex and difficult to predict. Laminar flows (and even stagnant waters) occur in dead-end pipes that connect to households or other withdrawal points (Buchberger and Wu, 1995). However, turbulent flows generally prevail in most locations, where $R > 10{,}000$. Turbulence is characterized by random and chaotic changes in the velocity field and flow patterns.

Despite these difficulties, numerous investigative projects have focused on proposing mathematical models to describe turbulence as well as analyzing the performance of such models in specific applications. Thakre and Joshi (2000) compared 14 versions of k–ε and Reynolds stress turbulence models to experimental data from heat transfer in pipe flows. They found that outcomes from k–ε turbulence models agreed better with experimental observations. Similar conclusions were drawn by Ekambara and Joshi (2003), who analyzed axial mixing in single pipe flows under turbulent conditions. In this work, the turbulence field was calculated using the k–ε model, which was composed of two equations that account for the turbulence kinetic energy [k, Eq. (5a)] and its rate of dissipation [ε, Eq. (5b)]:

$$\frac{\partial}{\partial x_i}(\rho k u_i) = \frac{\partial}{\partial x_j}\left[\left(\mu + \frac{\mu_t}{\sigma_k}\right)\frac{\partial k}{\partial x_j}\right] + G_k - \rho\varepsilon \tag{5a}$$

$$\frac{\partial}{\partial x_i}(\rho \varepsilon u_i) = \frac{\partial}{\partial x_j}\left[\left(\mu + \frac{\mu_t}{\sigma_\varepsilon}\right)\frac{\partial \varepsilon}{\partial x_j}\right] + C_{1\varepsilon}\frac{\varepsilon}{k}G_k - C_{2\varepsilon}\rho\frac{\varepsilon^2}{k} \tag{5b}$$

where the dimensionless constants for the turbulent model are: $C_{1\varepsilon}=1.44$, $C_{2\varepsilon}=1.92$, $C_\mu=0.09$, $\sigma_k=1.0$, and $\sigma_\varepsilon=1.3$. After the velocity and turbulence fields on the computational domain were obtained, the concentrations of NaCl were calculated using the species transport equation [Eq. (6)]. In steady-state, incompressible flows, the species transport equation is composed of two mechanisms: convective transport [due to bulk flow, the left-hand side of Eq. (6)] and diffusion [due to concentration gradients, the right-hand side of Eq. (6)],

$$\rho \nabla \cdot (\bar{u}C_i) = \nabla \cdot \left(\rho D_{AB} + \frac{\mu_t}{Sc_t}\right)\nabla C_i \tag{6}$$

The diffusion of species throughout the simulated region is modeled as the superposition of both molecular and eddy diffusivity; the latter is commonly known as dispersion. Molecular diffusion is a natural, dynamic process that tends to equilibrate the concentration of species. Even though D_{AB} (molecular diffusivity of Species A into Medium B) depends on temperature and aggregation of solute, among other factors, its value is known for typical solutions such as NaCl in water. On the other hand, eddy diffusivity depends on flow turbulence rather than the chemistry of species. Under fully turbulent flows, eddy diffusivity overwhelms molecular diffusivity by several orders of magnitude. Thus, NaCl mixing at cross intersections is mostly driven by diffusion caused by turbulence. In the CFD simulations presented here, the prediction of NaCl concentrations was dictated by the turbulent Schmidt number (Sc_t), which established the relationship between the turbulent transfer of momentum (μ_t) and the eddy diffusivity (D_t) as follows:

$$Sc_t = \frac{\mu_t}{\rho D_t} \tag{7}$$

Numerical setup

Numerical simulations of flows at cross junctions were performed using FLUENT (Fluent Inc. 2005a), a commercial CFD package based on the finite volume technique. This package uses GAMBIT (Fluent Inc. 2005b) as the preprocessor to create the geometries and meshes of the simulated physical space. Next, the conservation equations from Eq. (3) to Eq. (7) are discretized over the mesh computational domain, for which boundary conditions and material properties must be defined. The two inlets were defined as "velocity inlets" with uniform NaCl concentration profiles at each inlet. Flow rates at the two outlets were assigned based on $R_{E/N}$. A list of the set boundary conditions and their mathematical definitions is provided in Table 1. The material was set as a mixture composed of two constituent species: water ($\rho = 997$ kg m^{-3}, molecular weight=18.01 kg kg mol^{-1}) and NaCl ($\rho = 2{,}170$ kg m^{-3}, molecular weight=58.45 kg kg mol^{-1}). The varying mixture function depended upon the concentration of sodium chloride in water (volume weighted mixing law) and the dynamic viscosity was $\mu = 1 \times 10^{-3}$ kg m^{-1} s^{-1}. The molecular diffusion of NaCL in water was set equal to 1.5×10^{-9} m^2 s^{-1}. These material properties remained the same for all the simulations.

Table 1. Boundary Conditions for Numerical Simulation of the Cross Junction

Boundary	Velocity BC	Turbulence BC	Species BC
West inlet	$u=u_o, v=0$	$I=I_o, L=D$	$C=0$
South inlet	$u=0, v=v_o$	$I=I_o, L=D$	$C=C_o$
East outlet	$\frac{\partial u}{\partial x}=0, \frac{\partial v}{\partial x}=0$	$\frac{\partial k}{\partial x}=0, \frac{\partial \varepsilon}{\partial x}=0$	$\frac{\partial C_i}{\partial x}=0$
North outlet	$\frac{\partial u}{\partial y}=0, \frac{\partial v}{\partial y}=0$	$\frac{\partial k}{\partial y}=0, \frac{\partial \varepsilon}{\partial y}=0$	$\frac{\partial C_i}{\partial y}=0$
Walls	$u=0, v=0$	Enhanced wall treatment	$\frac{\partial C_i}{\partial n}=0$[a]

[a] n=normal vector to the wall.

Because several parameters of the numerical setup significantly affect the CFD outcomes even under the same flow and water quality configurations, careful analyses of these parameters are needed in order to ensure that they do not become a source of error. Such parameters include convergence criteria, mesh size, distribution of nonuniform mesh, discretization schemes, etc.

Convergence criteria are prescribed error tolerances for the scaled residuals of the conservation equations. The discretization of the conservation equation for any modeled variable ϕ (x, y velocity, species, kinetic energy, etc.) results in an algebraic equation, as expressed in Eq. (8). In this equation, a_P and ϕ_P=coefficient and value of the variable ϕ at the cell center, respectively, whereas a_{nb} and ϕ_{nb} come from the influencing neighbor cells and b is mostly influenced by the boundary conditions and source terms,

$$a_P\phi_P = \sum_{nb} a_{nb}\phi_{nb} + b \tag{8}$$

For every iteration, the solver provides a solution for the resulting set of algebraic equations for all the conservation variables ϕ. From such a solution, Eq. (8) does not hold true; instead, there is an imbalance that has to be quantified by subtracting the left-hand side from the right-hand side of Eq. (8). The imbalances from all the mesh cells are then added up and scaled, as expressed in Eq. (9). The iteration process stops when the scaled residual of the variable ϕ satisfies the prescribed convergence criteria. In order to test the optimal value that was used for further simulations, the convergence criteria were set equal for all the conservation equations; these ranged from 10^{-2} to 10^{-7},

$$R^{\phi} = \frac{\sum_{\text{cells } P} \left| \sum_{nb} a_{nb}\phi_{nb} + b - a_P\phi_P \right|}{\sum_{\text{cells } P} |a_P\phi_P|} \leq \text{convergence criterion} \tag{9}$$

Among the characteristics of the computational mesh, the shape and number of elements are the most relevant parameters for accuracy. In this work, several mesh sizes were tested in order to define their influence on the numerical solution. The mesh size ranged from 2,064 elements [the mesh size used by van Bloemen Waanders et al. (2005) with MP Salsa based on the finite element method] up to 80,064 for two-dimensional (2D) problems. An optimal mesh size produces no noticeable change in the outcomes corresponding to increased elements. Because the geometry of the pipes was very regular, quadrilateral elements were used over the entire computational domain and finer cells were drawn adjacent to the wall, with gradual enlargement at locations far from the wall (Romero-Gomez et al., 2006).

Numerical methods applied to the conservation equations are based on several discretization techniques. A particular technique has a set of corresponding solutions. Whereas in some applications, CFD simulations exhibit the same solution regardless of the set discretization technique, in other applications the CFD outcomes are markedly influenced by this setting. Therefore four schemes, First-order Upwind, Second-order Upwind, Quick, and Power Law schemes (Fluent Inc. 2005a), were tested when the Reynolds number was equal to 44,000 at all inlets and outlets. This particular Reynolds number (44,000) was chosen because of the experimental data (van Bloemen Waanders et al. 2005) available at the beginning of the present study. The aim was to quantify the effect of each scheme on the dimensionless concentration at both outlets as well as to select one to be used in further simulations.

Most physical processes occur naturally in three-dimensinal (3D) spaces; however, a recurring question in numerical modeling is whether 2D CFD simulations produce outcomes that are essentially equal to those obtained on 3D discretizations. Dropping one independent spatial variable not only simplifies the conservation equations to be manipulated, but also dramatically reduces the computational time spent to obtain the solution. Thus, a 3D mesh of the computational domain with 109,824 elements was created and simulations were performed in order to compare the outcomes to analogous 2D CFD results (Romero-Gomez et al. 2006). For this purpose, Scenario 1 (recall, equal inflows and outflows, $R_S=R_W=R_N=R_E$) was tested when the Reynolds number ranged from 11,000 to 88,000. The 3D boundary conditions remained the same as for the 2D scheme.

Turbulent flow at cross junctions is induced by different means. The ratio of wall roughness to pipe diameter contributes to increased turbulence intensity, mainly for long pipes. Because wall surfaces were assumed to be smooth throughout this study and the computational domain did not allow for the development of high turbulence due to wall roughness, this turbulence source was not relevant. On the other hand, because fittings create changes in geometry by creating either gaps or bumps that change turbulence intensity and the corresponding NaCl mixing ratio, fittings are localized sources of turbulence present at cross junctions. For this reason, the following sizes of bumps were examined by creating a geometrical shape as depicted in Fig. 2 (see the inset): $D_b/D=0.84$, 0.92, 0.96, and 0.98. Further, the following locations (L_b/D) of a bump of size $D_b/D=0.96$ were tested: 1.5, 1, 0.5, and 0.25 for Scenario 1. For all these simulations, the dimensionless concentration at both outlets was computed and plotted in order to determine whether the location and size of bumps had any effect on NaCl mixing. The width of the bump (W_b/D) was also considered as one of the parameters. The CFD package has several physical models available, and the users can examine or select a model depending on the specific modeling needs. For this reason, a thorough study was conducted to examine the accuracy of solutions for four benchmark problems with known analytical solutions and/or experimental data (Romero-Gomez et al. 2006). For instance, enhanced wall treatment was used instead of wall functions because enhanced wall treatment performed better when analyzing turbulent boundary layers, and based on the benchmarking results, its application proved to be more generalized than wall functions.

An analysis of dimensionless concentration based on the number of cells at the east outlet indicated that the optimal number of cells on the 2D simulation was about 60,000 cells (Romero-Gomez et al. 2006). The 2D results were compared with those for a 3D geometry with 110,000 cells, as shown in Fig. 1(c). The 2D and 3D simulation outcomes remained nearly the same, and the computational time is drastically reduced when 2D geometry is

used. Thus, all the simulations in the present study are conducted with 60,000 control volumes for the 2D geometry. A nonuniform mesh was carefully constructed and finer cells were used near the walls and the mixing zone due to larger gradients of the velocity, turbulence, and species fields. Approximately 30% of the cells were defined as "boundary layer cells," on which enhanced treatment of the conservation equations was applied.

Numerical Simulations

Scenario 1 is the most idealized case; all the inlet and outlet pipes have the same Reynolds number. Simulations were performed for the following Reynolds numbers to examine the effect of the flow speed on the mixing phenomena: 11,000 (u_o=0.218 m s^{-1}), 22,000 (u_o=0.436 m s^{-1}), 44,000 (u_o=0.874 m s^{-1}), and 88,000 (u_o=1.743 m s^{-1}). The "split" mixing ratio remains approximately constant based on numerical and experimental test runs in this R range (i.e., R > 11,000, the turbulent regime). The range of Reynolds number for the present study (R ≥ 11,000) is justified, as the majority of water distribution systems operate in the turbulent regime.

Scenario II (recall equal outflows and varying inflows, $R_S \neq R_W, R_N = R_E$) examines the Reynolds number ratios at the inlets while maintaining the same Reynolds numbers for both outlets. In all cases the flows were turbulent, and the specific Reynolds numbers set at the pipes are given in Table 2. Scenario III (equal inflows and varying outflows, $R_S = R_W, R_N \neq R_E$) was set up in a similar manner based on equal inflow and varying outflow conditions.

Thus far, species transport simulations were uncoupled with the momentum and mass conservation models. Physically, this approach means that the species concentrations do not affect the flow patterns, i.e., the species of study (NaCl) is considered a passive scalar. In the species transport model defined in Eq. (6), the total diffusivity is composed of the molecular and eddy diffusivities. Eddy diffusivity is calculated through the turbulent Schmidt number and the definition is given in Eq. (7). Therefore, eddy diffusivity is directly proportional to the eddy viscosity computed at each node and inversely proportional to the Sc_t. The aforementioned simulations were performed using the default value assigned to the turbulent Schmidt number (Sc_t=0.7). However, no universal relationship between turbulent momentum and species diffusivity exists. Therefore, comparisons of CFD outcomes to experimental data from Austin et al. (2008) helped to find the Sc_t numbers that governed the mixing process under investigation. This was completed by iterative processes based on experimental data for the generalized case ($R_S \neq R_W \neq R_N \neq R_E$). For each experimental data point, the actual Reynolds numbers for the four pipes and their corresponding velocities were extracted and set at the boundary conditions. After a CFD simulation was performed, the dimensionless concentrations at both outlets were obtained. If the simulated NaCl concentrations differed largely from experimental measurements, the Sc_t was updated and the simulation was run again. This update of Sc_t continued until the difference was less than the tolerance error (0.02).

Results and Discussion

Numerical Analysis

The required computational time is estimated based on the convergence criteria set. Any decrease in the convergence criteria conveys a significant increase in the time needed to obtain the results. Consequently, after a set of convergence criteria were tested, the results indicated that the minimum value of R^{ϕ} [Eq. (9)] to be used was 10^{-3} for all the conservation equations, as further decreases did not produce any significant changes in the results. The four tested discretization methods produced no substantial differences in dimensionless concentration at the outlets (less than 3%). The first order scheme produced higher mixing whereas the second order and Quick schemes both produced similar outcomes that indicated less mixing. Because a scheme that provides higher-order accuracy is preferable, the second order scheme was used for all subsequent simulations; this resulted in lowered computational time to perform simulations as compared to the Quick scheme.

The implementation of a bump due to fittings induced no significant increased mixing at the junction. Even when the diameter was reduced by 16% (D_b/D=0.84, L_b/D=1, and W_b/D=0.1), C_E^* did not change significantly (about 2%). Thus, it is assumed that the influence of fittings on the mixing is relatively small when the flow rates are nearly equal (Scenario 1).

Table 2. Reynolds Numbers at the Inlets and Outlets for Scenario 2

$R_{S/W}$	R_S	R_W	R_E	R_N
1	11,000	11,000	11,000	11,000
2	22,000	11,000	16,500	16,500
4	44,000	11,000	27,500	27,500
8	88,000	11,000	49,500	49,500
0.5	11,000	22,000	16,000	16,000
1	22,000	22,000	22,000	22,000
2	44,000	22,000	33,000	33,000
4	88,000	22,000	55,000	55,000
0.25	11,000	44,000	27,500	27,500
0.5	22,000	44,000	33,000	33,000
1	44,000	44,000	44,000	44,000
2	88,000	44,000	66,000	66,000
0.125	11,000	88,000	49,500	49,500
0.25	22,000	88,000	55,000	55,000
0.5	44,000	88,000	66,000	66,000
1	88,000	88,000	88,000	88,000

Flow Patterns and Concentration Contours

A major advantage of the CFD approach is that it enabled us to analyze and visualize flow and mass transport phenomena in detail. For instance, Figs. 3(a and b) show the velocity vectors and NaCl concentration contours (C^*), respectively, when the $R_S = R_W = R_E = R_N$=44,000 (i.e., Scenario 1), and D=2 in (5.08 cm). The NaCl dimensionless concentration ranges from 0 to 1 throughout the domain and the largest gradients occur where the two incoming flows merge along the line AB in Fig. 3(b), where the actual mixing of the two sources of water occurs. The water at high concentrations (south inlet) interacts over a very narrow mixing interface, the "impinging interface" (Ho et al. 2006), with the incoming pure water (left inlet), as if two impinging jets reflected off of the interface AB as shown in Fig. 3(a). The velocity vectors in the computational domain are nearly symmetrical with respect to line AB because the hydraulic conditions at the inlets and outlets are the same for this particular case (Scenario 1). However, dynamic boundary conditions and/or other turbulence modeling approaches produce nonsymmetrical velocity vectors, as presented by Webb and van Bloemen Waanders

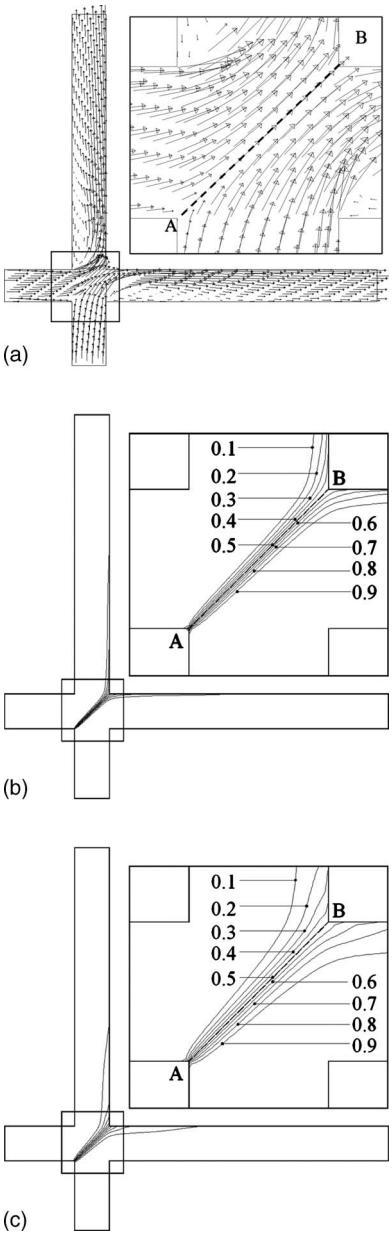

Fig. 3. Flow and concentration visualization for Scenario 1 at $R=44{,}000$: (a) Velocity vectors; (b) contours of NaCl dimensionless concentration with default $Sc_t=0.7$; and (c) contours of NaCl dimensionless concentration with corrected $Sc_t=0.1875$

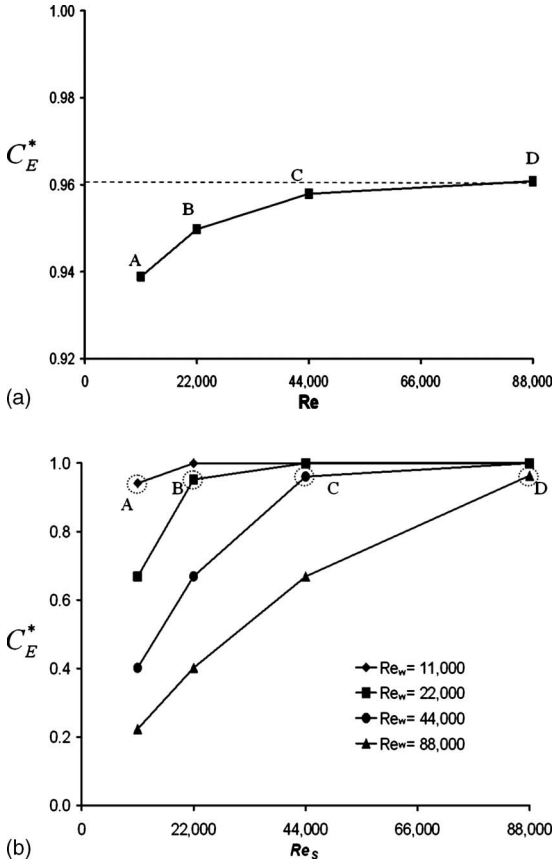

Fig. 4. Effects of the Reynolds number in dimensionless concentration at the east outlet: (a) Results for Scenario 1; (b) C_E^* as a function of Reynolds number at the south inlet (R_S) for Scenario 2. The data points (A, B, C, and D) that correspond to (a) are circled in (b).

(2006). It is evident that the limited instantaneous interaction between the two sources of water is the reason why the complete mixing assumption fails to represent the actual transport phenomena occurring at the cross junction. Another fundamental reason comes from the scaling factor (the turbulent Schmidt number Sc_t) that links the velocity and turbulent numerical fields with the species transport in this limited mixing zone. As expressed in Eq. (7), decreasing the turbulent Schmidt number (Sc_t) or increasing eddy viscosity (μ_t) is one way to enhance turbulent eddies.

Fig. 3(c) depicts the resulting contours of the NaCl dimensionless concentration (C^*) with an adjusted Sc_t based on the experimental data. In this case, the turbulent Schmidt number was modified iteratively until the CFD outcomes matched the experimental results obtained for that case (Scenario 1) by Austin et al. (2008). This scaling parameter does not modify the velocity field obtained previously and shown in Fig. 3(a). However, the contours in Fig. 3(c) show a wider strip that implies enhanced eddy diffusivity, and the enhanced mixing results in greater interaction between the two water sources.

Four Illustrated Scenarios

The dimensionless concentrations under the same R numbers at the inlets and outlets (Scenario 1) are depicted in Fig. 4(a). Again, the default value of the Schmidt number ($Sc_t=0.7$) is used to observe the overall trend. This trend is the result of two effects that act at the intersection of both incoming flows. On the one hand, higher R numbers produced larger velocities, which consequently induced higher eddy diffusivity at the interface. But unexpectedly, no monotonic decrease in dimensionless concentration is observed in Fig. 4(a). Instead, the curve increases steadily until it gradually approaches an asymptote ($C_E^* \rightarrow 0.96$) when $R>40{,}000$, revealing the relevance of the interaction time spent by both incoming flows of water at the interface. This interaction time was lower at higher R numbers, reducing the capacity for eddies to induce higher mixing between the high and low concentrations of water. This finding along with the observations from Fig. 3 clearly shows that both the interaction time and space have a significant effect on mixing at the junction.

It should be noted that the difference in dimensionless concentrations was only about 2% over the studied R number range

($11{,}000 \leq R \leq 88{,}000$). From a research standpoint, the variation of dimensionless concentration with respect to the Reynolds number must be analyzed in order to obtain a better understanding of the physical models used in transport phenomena within pressurized pipe systems. From a practical standpoint, however, considering the uncertainties in real distribution systems, this difference may be ignored in order to simplify modeling. The dimensionless concentration can be assumed to be constant at 0.95 when $R \geq 10{,}000$. This assumption is not valid in laminar and transitional regimes, and further investigations are necessary over broader R number ranges.

After simulations of Scenario 2 (Table 2), different Reynolds numbers at two inlets (south and west) were used to plot a series of curves of the dimensionless concentration at the east outlet, as depicted in Fig. 4(b). For each curve, the amount of low concentration water was held constant whereas the flow of high concentration water was increased. As a consequence, dimensionless concentrations were higher as R_S increased. The data points (*A*, *B*, *C*, and *D*) that correspond to Fig. 4(a) are circled in Fig. 4(b) to demonstrate that Scenario 1 is a specific case of Scenario 2. It is clear that the Reynolds number ratio of two inlets is the dominant factor of the solute concentration split at the cross junction. Therefore, the general trend in Fig. 4(b) can be better summarized using the R ratio of the inlets ($R_{S/W}$) and the dimensionless concentration to the east outlet (C_E^*) at various R_W, the results of which are presented in Fig. 5, again with $Sc_t = 0.7$.

The curves are nearly overlapping each other. Slight differences are observed at $R_{S/W} = 1$ at various R_W, particularly at the lower limits (11,000 and 22,000). The largest difference can be observed between the curves for $R_W = 11{,}000$ to 22,000, whereas the curves remain essentially the same in the transition from $R_W = 44{,}000$ to 88,000. For Scenario 1 ($R_{S/W} = 1$, a special case of Scenario 2), the trend was clearly shown in Fig. 4(a). No change is expected if curves of $R_W > 88{,}000$ were plotted. From the results obtained outside of the range $0.7 < R_{S/N} < 1.7$, mixing at cross junctions is mainly driven by ratios of Reynolds numbers, rather than Reynolds numbers explicitly. For the entire $R_{S/W}$ of the given scenario, it is likely that the difference is negligible for real-world water quality modeling practices as long as R_W remains greater than 10,000. A similar exemplary case can be described for Scenario 3, though for brevity, the case is not presented here.

In Fig. 5, point α corresponds to the instance when $R_S = 10{,}478$ and $R_W = 52{,}393$ ($R_{S/N} = 0.25$), whereas point β corresponds to the case when $R_S = 47{,}154$ and $R_W = 15{,}718$ ($R_{S/N} = 3$). The visualization of NaCl dimensionless concentration contours and velocity vectors for both cases are presented in Fig. 6. The complete mixing assumption indicates that the water flows have enough interaction to flow out with the same concentration. However, for α, high concentration water is swept out mostly to the east outlet because the momentum of the low concentration flow is larger, and entrains the NaCl coming from the South inlet [Figs. 6(a and b), $Sc_t = 0.0468$]. On the other hand, point β represents the case when larger volumes of high concentration water sweep the low concentration water flow through the north outlet without allowing for interactions that could lower the concentration at the east outlet [Figs. 6(c and d), $Sc_t = 0.125$]. It is clear that the flow rate ratio is the driving force that determines the mixing patterns at cross junctions.

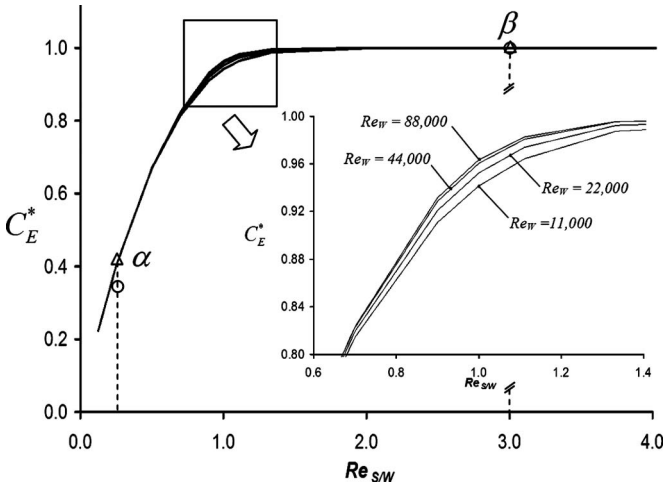

Fig. 5. Dimensionless concentration at the east outlet as a function of ratio of Reynolds numbers of both inlets ($R_{S/W}$), when $Sc_t = 0.7$. Triangle points α and β are calculated when $R_{S/W} = 0.25$ and 3.0, respectively. Circular points are calculated with corrected Schmidt numbers based on experimental results, i.e., $Sc_t = 0.046$ and 0.125, respectively, when $R_{S/W} = 0.25$ and 3.0.

Adjustment of the Schmidt Number

It was postulated that the turbulent Schmidt number (Sc_t) has a major influence on the instantaneous mixing phenomena along the mixing zone, as discussed earlier. All the preceding simulations were performed with $Sc_t = 0.7$, which is the default value assigned by FLUENT when the k–ε turbulence model is used. However, Austin et al. (2008) compared CFD and experimental NaCl dimensionless concentrations for Scenario 2 and found that CFD values were overestimated (over the analyzed range of $R_{S/W}$), with a maximum error of about 8% with respect to experimental measurements. Thus, this study suggests that the Sc_t should be corrected over a set of experimental data points.

The generalized case of different R numbers for inlets and outlets was investigated experimentally by Austin et al. (2008). A total of 49 cases with three repetitions were carried out, and their results were used in this study to map the turbulent Schmidt number that best fit each combination of R numbers tested. The contours of the fitted turbulent Schmidt numbers are shown in Fig. 7. Fig. 7 also includes the locations of three example cases (α and β in Fig. 5 and Scenario 1). Even though a large range of Sc_t ($0.03 < Sc_t < 1$) produced the CFD outcomes that matched experimental data, some trends over the chart are manifest. The dimensionless concentrations have values near 1 for $R_{E/N} \sim 0$ (bottom edge), whereas low values ($0.03 < Sc_t < 0.2$) are observed along the left edge ($R_{S/W} \sim 0$) and most of the right edge ($R_{S/W} \sim 4$, and $R_{S/W} > 1$). Contours for low dimensionless concentrations ($0.1 < Sc_t < 0.2$) prevail over most of the central region of the area ($0.5 < R_{S/W} < 3.5$ and $1 < R_{E/N} < 3$).

Although experimental data were obtained for $0.25 \leq R_{S/W} \leq 4$ and $0.25 \leq R_{E/N} \leq 4$, actual flows in water distributions systems can reach beyond that range. General trends beyond this range can be assessed via extrapolation of the experimental results as shown in Fig. 8. Scenario 1 and cases α and β used in Fig. 5 are also presented for the purpose of comparison. However, flow in one of four pipe legs is likely in laminar and transitional regimes as $R_{S/W}$ or $R_{E/N}$ approaches the two extreme limits (0 and ∞). Thus, it is important to note that Fig. 8 should be used for water quality modeling only if $R > 10{,}000$.

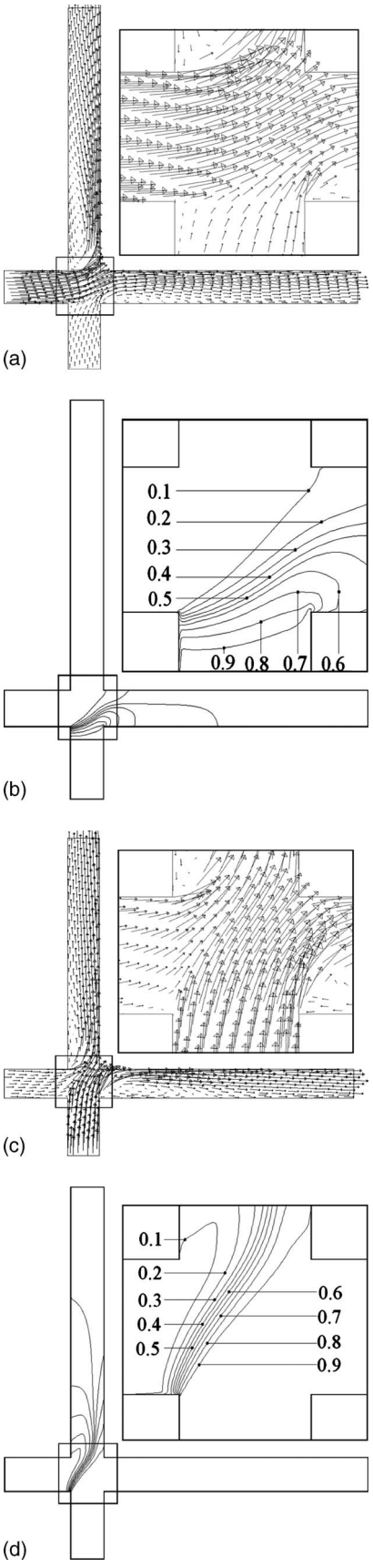

Fig. 6. Flow and concentration visualization at α and β (see Fig. 5) with corrected Sc_t: (a) Velocity vectors at α; (b) C^* contours at α (Sc_t=0.0468); (c) velocity vectors at β; and (d) C^* contours at β(Sc_t=0.125)

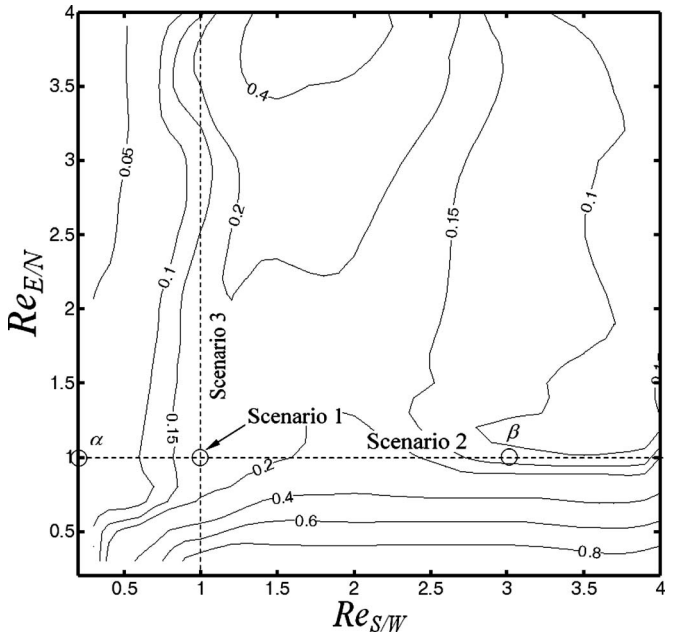

Fig. 7. Contour of fitted turbulent Schmidt number (Sc_t) as a function of both $R_{S/W}$ and $R_{E/N}$ based on experimental results by Austin et al. (2008). See Fig. 5 for α and β.

In the present study, the Reynolds numbers (Re) is considered as the primary dimensionless parameter. However, the Reynolds number may not account for all scaling factors under various conditions. For example, with larger pipe diameters, the flow velocity will be significantly smaller than the velocities used in the experiments for the same Reynolds number. A slower velocity and larger pipe diameter would increase contact time, contact area, and potentially the amount of mixing when compared to mixing in smaller pipes with higher velocities at the same Rey-

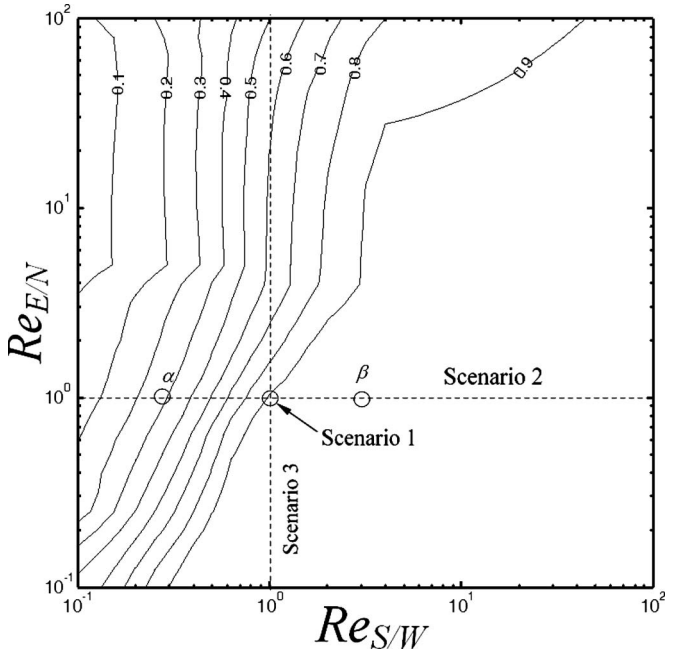

Fig. 8. Contours of dimensionless concentrations at the east outlet (C_E^*) extrapolated over $R_{S/W}>4$ and $R_{E/N}>4$. See Fig. 5 for α and β.

nolds number. A few cases were examined with several pipe diameters (ID at 12.7, 19.1, and 50.8 mm) at the same Reynolds number with a constant diffusivity (NaCl), and the mixing ratio remained the same for all cases. The outcome may change when highly diffusive solutes flow in a large water main at a low flow rate. In this case, the molecular diffusivity of a solute may play a significant role for the mixing ratio. However, it would be rare to observe low flow rates in water mains. It should also be noted that the RANS model used for the present investigation may not be able to capture potentially transient behaviors at the cross junction. To address these issues, further studies are recommended using flow visualization and high-fidelity computational techniques such as large eddy simulation and direct numerical simulation.

Conclusions

The representation of solute mixing behavior at pipe junctions impacts a wide variety of water distribution network analyses, including prediction of disinfectant residuals, optimal locations for water quality sensors, prediction models for early warning systems, numerical schemes for inverse source identification, and quantitative risk assessment. The present study addressed solute mixing phenomena at four-pipe cross junctions, which are commonly found in municipal drinking water distribution systems. Simulations using CFD were employed to understand mixing mechanisms at the junction and to examine the general trend of percent solute splits. Experimental results were used to assess representative Sc_t numbers for various flow conditions. The present study indicates that mixing at pipe cross junctions is far from "perfect." Incomplete mixing results from bifurcating inlet flows that reflect off of one another with minimal contact time. Additional experiments and computational studies are necessary to understand the mixing phenomena of flows ranging from laminar to transitional to turbulent flows at cross junctions.

Acknowledgments

This work is supported by the Environmental Protection Agency/Department of Homeland Security (under Grant No. 613383D). Sandia is a multiprogram laboratory operated by Sandia Corporation, a Lockheed Martin Company for the United States Department of Energy's National Nuclear Security Administration under Contract No. DE-AC04-94AL85000. We would like to acknowledge collaborators at Tucson Water (Dan Quintanar and Dean Trammel) who have contributed their valuable time and efforts to the present work.

Notation

The following symbols are used in this paper:

a_{ab} = coefficient at influencing neighbor cell;
a_P = coefficient at cell center;
b = coefficient influenced by boundary conditions and source terms;
C = NaCl concentration, kg kg^{-1};
C^* = dimensionless concentration;
C_i = NaCl concentration at ith cell;
D = pipe diameter, m;
D_{AB} = molecular diffusivity, m^2 s;
D_b = reduced pipe diameter, m;
D_t = eddy diffusivity, m^2 s;
G_k = generation of turbulence kinetic energy, kg m^{-1} s^{-3};
I = turbulence intensity, %;
k = turbulence kinetic energy, m^2 s^{-2};
L = hydraulic diameter, m;
L_b = distance of bump from pipe intersection, m;
P = pressure, Pa;
R = Reynolds number, $\rho DU/\mu$;
R^ϕ = residual of conservation variable ϕ;
Sc_t = turbulent Schmidt number, $\mu_t/\rho D_t$;
U = average pipe flow velocity, m s^{-1};
u = x-velocity component, m s^{-1};
$\bar{u}$ = velocity vector, m s^{-1};
u_i = ith velocity component at cell center, m s^{-1};
v = y-velocity component, m s^{-1};
W_b = bump length, m;
ε = turbulence dissipation rate, m^{-2} s^{-3};
μ = molecular viscosity, kg m^{-1} s^{-1};
μ_t = eddy viscosity, kg m^{-1} s^{-1};
ρ = mixture density, kg m^{-3};
$\bar{\bar{\tau}}$ = stress tensor, kg m^{-1} s^{-2};
ϕ_{ab} = conservation variable at influencing neighbor cell; and
ϕ_P = conservation variable at cell center.

Subscripts

E = east outlet;
E/N = ratio of outlets, east to north;
N = north inlet;
S = south inlet;
S/W = ratio of inlets, south to west; and
W = west inlet.

References

Austin, R. G., van Bloemen Waanders, B., McKenna, S., and Choi, C. Y. (2008). "Mixing at cross junctions in water distribution systems. II: Experimental study." *J. Water Resour. Plann. Manage.*, 134(3), 295–302.

Buchberger, S. G., and Wu, L. (1995). "Model for instantaneous residential water demands." *J. Hydraul. Eng.*, 121(3), 232–246.

Ekambara, K., and Joshi, J. B. (2003). "Axial mixing in pipe flows: Turbulent and transition regions." *Chem. Eng. Sci.*, 58(12), 2715–2724.

Fluent Inc. (2005a). *Fluent 6.2 user's guide*, Lebanon, N.H.

Fluent Inc. (2005b). *Gambit 2.2 user's guide*, Lebanon, N.H.

Fowler, A. G., and Jones, P. (1991). "Simulation of water quality in water distribution systems." *Proc. Water Quality Modeling in Distribution Systems*, AwwaRF/EPA, Cincinnati.

Ho, C. K., Orear, L., Wright, J. L., and McKenna, S. A. (2006). "Contaminant mixing at pipe joints: Comparison between laboratory flow experiments and computational fluid dynamics models." *Proc. 8th Annual Water Distribution System Analysis Symp.*, Cincinnati.

Mays, L. W. (2004). *Water supply systems security*, McGraw-Hill Professional, New York.

Romero-Gomez, P. Choi, C. Y., van Bloemen Waanders, B., and McKenna, S. A. (2006). "Transport phenomena at intersections of pressurized pipe systems." *Proc. 8th Annual Water Distribution System Analysis Symp.*, Cincinnati.

Rossman, L. (2000). *EPANET user's manual*, USEPA, Cincinnati.
Thakre, S. S., and Joshi, J. B. (2000). "CFD modeling of heat transfer in turbulent pipe flows." *AIChE J.*, 46(9), 1798–1812.
van Bloemen Waanders, B., Hammond, G., Shadid, J., Collis, S., and Murray, R. (2005). "A comparison of Navier-Stokes and network models to predict chemical transport in municipal water distribution systems." *Proc., World Water and Environmental Resources Congress*, Anchorage, Alaska.
Webb, S. W., and van Bloemen Waanders, B. G. (2006). "High fidelity computational fluid dynamics for mixing in water distribution systems." *Proc. 8th Annual Water Distribution System Analysis Symp.*, Cincinnati.